Applied Ocean Research 51 (2015) 14–24

Contents lists available at ScienceDirect

Applied Ocean Research

journal homepage: www.elsevier.com/locate/apor

Numerical investigation of the hydrodynamic interaction between two underwater bodies in relative motion

S.A.T. Randeni P.[a,*], Z.Q. Leong[a], D. Ranmuthugala[a], A.L. Forrest[a,b], J. Duffy[a]

[a] Australian Maritime College, University of Tasmania, Launceston, Australia
[b] Tahoe Environmental Research Center, University of California – Davis, Incline Village, NV, USA

ARTICLE INFO

Article history:
Received 6 August 2014
Received in revised form 6 February 2015
Accepted 11 February 2015
Available online 10 March 2015

Keywords:
Underwater body interaction
Computational Fluid Dynamics
Autonomous Underwater Vehicles
Hydrodynamic coefficients
Manoeuvring simulations

ABSTRACT

The hydrodynamic interaction between an Autonomous Underwater Vehicle (AUV) manoeuvring in close proximity to a larger underwater vehicle can cause rapid changes in the motion of the AUV. This interaction can lead to mission failure and possible vehicle collision. Being self-piloted and comparatively small, an AUV is more susceptible to these interaction effects than the larger body. In an aim to predict the manoeuvring performance of an AUV under the effects of the interaction, the Australian Maritime College (AMC) has conducted a series of computer simulations and captive model experiments. A numerical model was developed to simulate pure sway motion of an AUV at different lateral and longitudinal positions relative to a larger underwater vehicle using Computational Fluid Dynamics (CFDs). The variables investigated include the surge force, sway force and the yaw moment coefficients acting on the AUV due to interaction effects, which were in turn validated against experimental results. A simplified method is presented to obtain the hydrodynamic coefficients of an AUV when operating close to a larger underwater body by transforming the single body hydrodynamic coefficients of the AUV using the steady-state interaction forces. This method is considerably less time consuming than traditional methods. Furthermore, the inverse of this method (i.e. to obtain the steady state interaction force) is also presented to obtain the steady-state interaction force at multiple lateral separations efficiently. Both the CFD model and the simplified methods have been validated against the experimental data and are capable of providing adequate interaction predictions. Such methods are critical for accurate prediction of vehicle performance under varying conditions present in real life.

1. Introduction

Autonomous Underwater Vehicles (AUVs) are used in civilian, academic, and military applications due to their ability to undertake complicated tasks underwater without real-time user control. A few examples of such applications include underwater surveillance [1] and sampling physical transport processes in lakes [2]. AUVs are increasingly required to operate close to larger underwater vehicles such as submarines and larger Remotely Operated Vehicles [3], as well as to operate in swarms of AUVs of similar size [4]. When operating in close proximity to a larger moving vehicle like a submarine, an AUV can experience motions resulting from the interaction of the wake and pressure fields generated by the larger body [5]. Being relatively small and self-piloted, the AUV is more susceptible to these interaction effects, which can result in mission failure and, in extreme cases collision between the two vehicles. For this reason, it is critical to understand the manoeuvring performance of an AUV under these interaction effects in order to develop adequate control strategies [6].

While there have been considerable studies on hydrodynamic interactions between surface ships [7–9], there is currently very little information on the interaction between submerged vessels in the public domain. Mawby et al. [10] developed a high level architecture model to simulate the interaction between a moving submarine and a rescue submersible manoeuvring to the escape hatch of the submarine. This earlier model utilized pre-processed hydrodynamic interaction data obtained by solving the Laplace's equation using a boundary element method for the inviscid, irrotational flow past the vehicles' surfaces. The limitation of the utilized potential flow approach is that it does not account for fluid viscosity or wake field effects of the vehicles and will potentially oversimplify the interaction effects.

Previous numerical and experimental studies by Leong et al. [6] have investigated the interaction effects on an AUV operating close to a larger vehicle for diameter ratios between the vehicles ranging from 2.237:1 up to 13.425:1 (i.e. displacement ratio from 10.419:1 to 139.878:1 respectively). The influence of different

* Corresponding author at: Locked Bag 1395, Launceston, TAS 7250, Australia. Tel.: +61 47 047 6942.
E-mail address: Supun.Randeni@utas.edu.au (S.A.T.R. P.).

0141-1187/$ – see front matter.
http://dx.doi.org/10.1016/j.apor.2015.02.006

Nomenclature

D	diameter of the body [m]
Fy	sway force [N]
Fy'	non-dimensional sway force coefficient, $\frac{2Fy}{\rho L^2 U^2}$
L	overall length of body [m]
L_S	surface length of body [m]
m	mass of body [kg]
N	Yaw moment [Nm]
N'	non-dimensional yaw moment coefficient, $\frac{2N}{\rho L^3 U^2}$
Re	Reynolds number
R_{lat}	lateral body separation ratio
R_{long}	longitudinal body separation ratio
u	forward velocity [m/s]
v	sway velocity [m/s]
$\dot{v}$	sway acceleration [m/s^2]
$y+$	non-dimensional distance from wall to first node
Y_v	sway force coefficient due to sway velocity [N]
$Y_{\dot{v}}$	sway force coefficient due to sway acceleration [N]
Δ	displacement [m^3]
ω	sway frequency [rad/s]

lateral and longitudinal distances between the two bodies over a range of speeds were investigated through Computational Fluid Dynamic (CFD) simulations and validated with captive model experiments [6]. Leong [11] also carried out dynamic CFD simulations, modelling the pure sway motion of a smaller AUV model in close proximity to a larger AUV at one relative longitudinal position.

The work presented in this paper complements this previous work by considering a larger range of longitudinal positions and sway motion frequencies, with the information presented for a diameter ratio of 2.237:1 (i.e. displacement ratio of 10.419:1). The authors have also extended the capabilities of the CFD numerical model to simulate pure yaw motion of the AUV in close proximity to a larger body; however, will not be presented in this work. The numerical model was developed in ANSYS-CFX, utilizing re-meshing techniques and was validated against experimental work conducted in the Towing Tank of the Australian Maritime College (AMC) at the University of Tasmania. Once validated, this numerical model can be extended to investigate the interaction between vehicles of larger diameter ratios, thus better representing the interaction between typical submarines and AUVs. A simplified method is presented to obtain the hydrodynamic coefficients of an AUV when operating close to a larger underwater body by transforming the single body hydrodynamic coefficients, using the steady state interaction forces. Using this method, the variation of hydrodynamic coefficients due to a second body could be estimated by conducting a less time consuming steady-state simulation, rather than time intensive dynamic pure sway motion simulations. Furthermore, the inverse of this method (i.e. to obtain the steady state interaction force) is also presented and validated. Inverse method is an efficient way of obtaining the steady-state interaction force at multiple lateral separations.

2. Methodology

2.1. Geometric models

The hydrodynamic characteristics of an AUV operating close to a larger underwater body were investigated through CFD and Experimental Fluid Dynamics (EFD) using two axisymmetric bare-hull underwater vehicle geometries. The research utilized a 1:2.801 scaled model of the SUBOFF submarine hullform developed by the Defence Advanced Research Projects Agency (DARPA) [12] as the smaller AUV, and a larger torpedo-shape body designated as NP01, with the principal dimensions of the models are shown in Fig. 1(a) and Table 1. The diameter ratio of the NP01 model to the SUBOFF model is 2.237:1. The model scales were selected to ensure that they were sufficiently small to fit within AMC's towing tank without causing blockage effects, but large enough to provide magnitudes of interaction forces that are larger than the experimental error levels.

Table 1
Principal particulars of the two models.

	SUBOFF model	NP01 model
Length (L)	1.438 m	2.850 m
Diameter (D)	0.181 m	0.410 m
Displacement (Δ)	0.031 m^3	0.323 m^3

2.2. Test parameters

The test runs consisted of straight-line and pure sway motions of the SUBOFF at different relative longitudinal and lateral positions to the larger NP01, with the investigated variables consisting of the surge force, sway force and the yaw moment experienced by the SUBOFF model. The lateral distance between centrelines of the two bodies was assumed to be the lateral separation distance, while the longitudinal separation distance was measured from the nose tip of the larger NP01 vehicle to that of the smaller SUBOFF vehicle; a 'positive' distance signifying that the SUBOFF model is located in front of the larger vehicle as shown in Fig. 1(a). The longitudinal and lateral distances were non-dimensionalized as follows:

$$\text{Longitudinal separation ratio } (R_{long}) = \frac{\text{Distance SUBOFF nose tip to NP01 nose tip}}{\text{Length of NP01}} \quad (1)$$

$$\text{Lateral separation ratio } (R_{lat}) = \frac{\text{Lateral separation distance}}{\text{Diameter of NP01}} \quad (2)$$

The coordinate system was selected according to [13] as shown in Fig. 1(b).

In order to isolate the interaction forces due to the larger second body, single body testings of the SUBOFF were conducted to provide baseline data. A summary of the single-body and two-body test parameters is outlined in Table 2. The estimated Reynolds number (Re_{L_S}) is based on the length of the SUBOFF model, which is 1.438 m.

2.3. Definition of test motions

2.3.1. Straight-line motion

In the straight-line motion experiments, the bodies were moved in an equal forward velocity with a zero angle of attack. The aim of these tests was to obtain the sway and drag forces on the smaller SUBOFF body due to the forward motion when it is alongside the larger body. The obtained forces are referred to as the forces due to 'steady state straight-line motion'.

2.3.2. Pure sway motion

In the pure sway motion experiments, the SUBOFF model was moved forward at a constant velocity while undergoing sinusoidal oscillations in the y direction around its centre line (see Fig. 2) in order to obtain the surge force, sway force and the yaw moment due to sway velocity and sway acceleration. The angle of attack was maintained at zero. In pure sway motion, the sway displacement (y) is 90° out-of-phase with the sway velocity (v). The sway acceleration ($\dot{v}$) is in-phase with the sway displacement, while being 90°

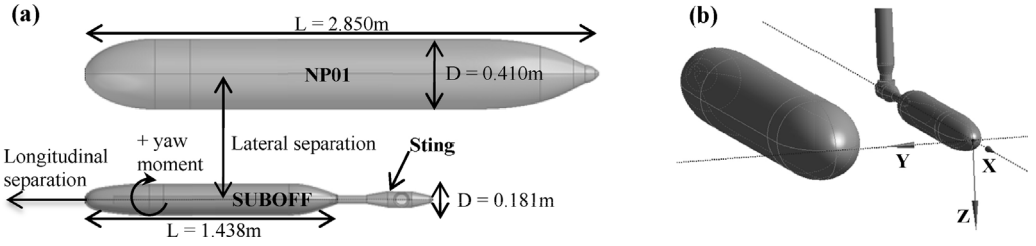

Fig. 1. (a) The SUBOFF model alongside the larger NP01 model indicating the model dimensions and test rig arrangement along with (b) the assumed coordinate system.

Table 2
Test programme.

Investigated parameters	Straight-line motion	Pure sway motion
Single body tests		
Sway amplitudes (m)	–	0.145
Sway frequency (Hz)	–	0.2, 0.15, and 0.05
Two body tests		
Sway amplitudes (m)	–	0.145
Sway frequency (Hz)	–	0.2, 0.15, and 0.05
Longitudinal separation ratios	0.737, 0.491, 0.246, 0, −0.246, −0.491, −0.737	0.737, 0.491, 0.246, 0, −0.246, −0.491, −0.737
Lateral separation ratio	1.829	1.829
Forward speed (m/s)	1.2	
Reynolds number$_{(Length)}$	19.39×10^5	
Forces measured	Surge force, sway force, and yaw moment	

out-of-phase with the sway velocity. The forces and moments acting on the SUBOFF model due to sway motion is composed of both inertial and damping components, with the former is dependent on the acceleration while the latter is dependent on the velocity. The acceleration dependent component of the sway force becomes zero when the force is 90° out-of-phase with the displacement (i.e. when the velocity is at its peak and the acceleration is zero). This is termed as the 'sway force due to sway velocity (Fy'_{out}), with its hydrodynamic coefficient obtained by differentiating Fy_{out} with respect to sway velocity [14] as shown in Eq. (3). Similarly, the acceleration component dominates when the sway force is in-phase with the displacement (Fy_{in}; i.e. when the acceleration is at its peak and the velocity is zero), with the coefficient (referred to as the added mass coefficient) obtained by differentiating Fy_{in} with respect to sway acceleration [14] as shown in Eq. (4).

$$Y_v = \frac{\partial Y}{\partial v} = \frac{Fy_{out}}{-a_0\omega} \tag{3}$$

$$Y_{\dot{v}} = \frac{\partial Y}{\partial \dot{v}} = \frac{Fy_{in}}{-a_0\omega^2} + m \tag{4}$$

where Y_v is the sway force coefficient due to sway velocity; $Y_{\dot{v}}$ is the sway force coefficient due to sway acceleration (added mass coefficient); a_0 is the sway amplitude; ω is the sway frequency; and m is the mass of the model.

3. Experimental setup

The captive model experiments were conducted in AMC's Towing Tank with the dynamic motion of the SUBOFF obtained using a Horizontal Planer Motion Mechanism (HPMM). The SUBOFF model was mounted to the HPMM using a 'sting', which connects to the model through the aft end as shown in Fig. 3(a). The forces acting on the SUBOFF model were recorded using two 6-Degree of Freedom (6-DOF) load cells positioned in-line with the force balance located inside the model. The force balance is an extension of the sting that connects to the model via the load cells as shown in Fig. 3(a). The SUBOFF model is not watertight, with vent holes allowing it to fill with water during testing. A gap in between the aft end of the model casing and the sting avoids contact between them eliminating friction and pre-tensioning effects. A Hama boundary layer transition strip device [15] was attached at 5% of the overall hull length aft of the model's leading edge to trip the laminar boundary layer into a turbulent one. The forces on the larger model were not recorded as modelling the larger vehicle was not an objective of this work. Fig. 3(b) shows the two models, with the NP01 attached to the towing tank carriage at an R_{lat} of 1.829. The NP01 had a 1 m gap from its longitudinal centreline to the nearest side wall and was shifted longitudinally to achieve the desired R_{long} between the bodies. The R_{lat} was obtained by moving the SUBOFF laterally using the HPMM.

The variation of forces acting on the SUBOFF model due to the free surface was investigated by Steel [16], concluding that the surface interference is negligible for non-dimensional depths of H/D greater than 3.3 (where H is the submerged depth from the surface waterline to the centreline of the vehicle as shown in Fig. 3(a), and D is the model diameter). For this reason, the vehicles were positioned 0.75 m below the waterline at mid-depth of the tank in order to minimize free surface effects as well as tank floor effects (i.e. the SUBOFF and the NP01 at non-dimensional depths of 4.147 and 1.852 respectively). The distance from the tank floor to the SUBOFF's and the NP01's bottom surface edges were 0.66 m and 0.55 m respectively. Further information with regard to the experimental setup is given in van Barneveld [17].

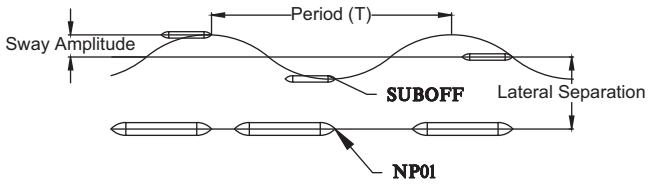

Fig. 2. SUBOFF model undergoing the pure sway motion close to the larger NP01.

4. Numerical simulations

To assist with the validation of CFD results against EFD, the width and depth of the AMC towing tank were replicated in the numerical fluid domain. The numerical domain length was reduced to 20 m

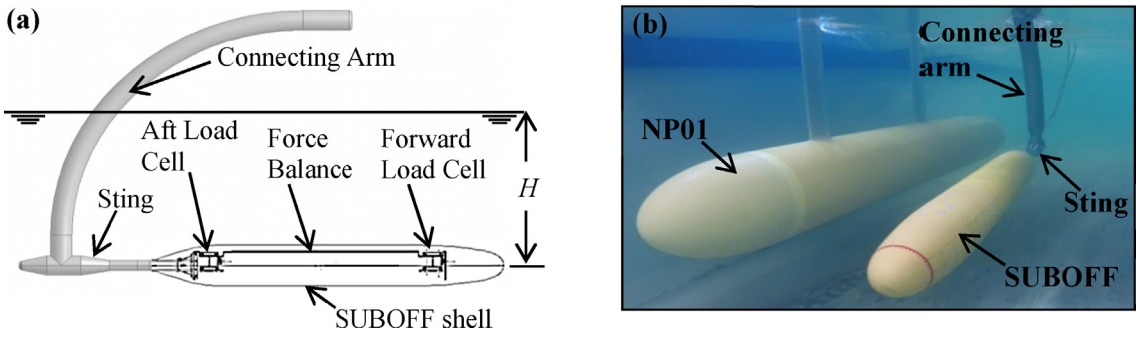

Fig. 3. Experimental set up of (a) the SUBOFF model and (b) both the SUBOFF and NP01 model together.

from the towing tank length of 100 m to reduce the computational effort while still capturing the wake field generated by the vehicles at the stern (see Fig. 4). Thus, it is assumed that reducing the modelled length of the towing tank has a negligible effect on the results.

In simulating the fluid flow around the submerged bodies, the Reynolds Averaged Navier Stokes (RANS) equations were utilized. Leong [18] evaluated the performance of two RANS-based turbulence models (i.e. Baseline Reynolds Stress Model (BSLRSM) and Shear Stress Transport with Curvature Correction (SSTCC)) in predicting the flow around the SUBOFF model and obtaining hydrodynamic coefficients under translation and rotational flow conditions. Leong [18] showed that the BSLRSM solution was the closest in comparison to the experimental results and was thus utilized in this investigation. This low Reynolds wall treatment model is recommended only when accurate prediction of separation wall-bounded flows are desired and $y^+ < 1$ (where y^+ is the non-dimensional value of the distance from the surface of the body to the first node of the mesh) is utilized, conditions that were adhered to in all simulations.

The ANSYS Meshing Platform (AMP) re-meshing method was used to simulate the relative motion between the two bodies. The essential aspect of this method is that the mesh in the fluid domain deforms locally around the moving object as it moves, and re-meshes when the mesh quality is deemed compromised in terms of accuracy and stability [19]. This overcomes the limited motions imposed by using a pure mesh deformation approach and allows rotation of the bodies to be compared to other re-meshing methods. Although mesh deformation is fully supported in ANSYS CFX, currently the re-meshing requires the use of a user-defined script. The latter, triggered by the mesh quality criterion, interrupts the simulation and transfers the positional state of the SUBOFF into ANSYS Workbench in order to update the geometry and the mesh. The script then transfers the new mesh into the solver where the simulation information from the previous mesh is interpolated into the new mesh and the simulation is resumed. The mesh quality criterion was defined as the orthogonality angle in the mesh cells of no less than 10° [11]. The fluid domain of the study was formed from three sub-domains (see Fig. 4): the SUBOFF sub-domain, the NP01 sub-domain and the tank domain. In order to reduce the re-mesh time, the vehicle sub-domains were pre-meshed and were kept rigid during the solver process, while the tank domain underwent mesh deformation and re-meshing.

4.1. Meshing

To aid the validation, the experimental setup was identically replicated by the CFD mesh model. The mounting arrangement of the SUBOFF model to the HPMM (i.e. the sting) can cause pressure field variations and generate an additional wake field. Thus, the sting arrangement was modelled in the CFD simulations. During the experiments, the internal hollow section of the SUBOFF shell was filled with water and, as the tests involved accelerative motions, the inertial effects produced by the water inside the SUBOFF model were proven to be significant. Therefore, the internal water was meshed and interfaced with the surrounding water as shown in Fig. 5 (inset). The inertial effects due to the mass of the SUBOFF's shell were modelled by defining the density of the shell material (i.e. fibreglass plastic) to the mesh within the shell. Predictions of the inertial forces may vary from exact physical values as the internal water volume and the mass of the SUBOFF shell cannot be accurately modelled due to the complexity of the force balance arrangement inside the shell and due to the uneven shell density.

It is well documented that the total thickness of the inflation prism layers should be at least the thickness of the boundary layer [20], where the inflation prism layer is a layer with very small mesh elements in the direction normal to the wall that resolves the wall region to aid the turbulent model to capture the boundary

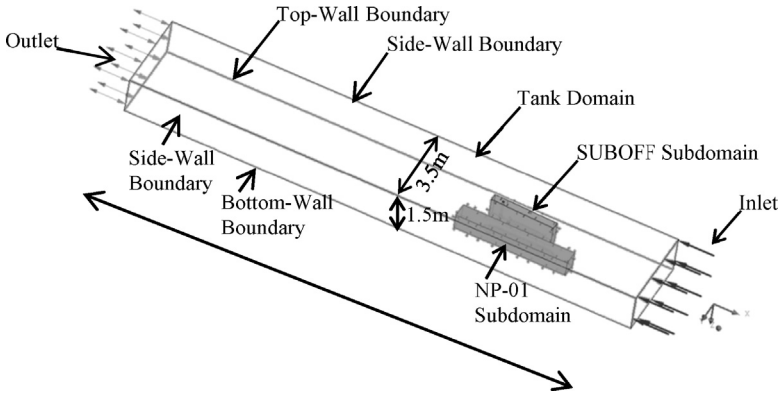

Fig. 4. Numerical fluid domain subdivided to represent the tank domain, SUBOFF subdomain and NP01 subdomain.

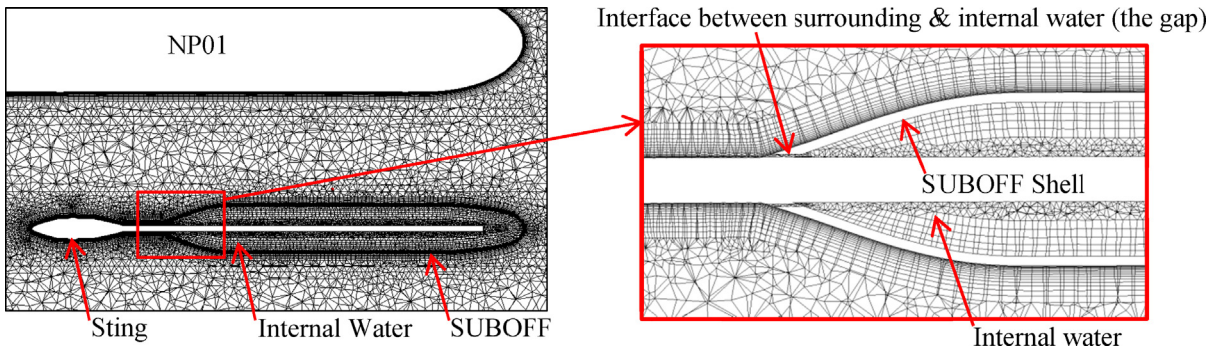

Fig. 5. Mesh model around the sting and two submerged model bodies and the internal water of the SUBOFF (inset) to closely replicate the EFD. The mesh of the SUBOFF shell is removed in the inset to provide a detail illustration of the interface gap.

layer [21]. If the thickness of the inflation prism layers is underprescribed, this will 'squash' the predicted boundary layer in the simulation and correspondingly affect the forces acting on the vehicle. Overprescribing the thickness does not affect the force predictions; however, it will increase the number of mesh elements. Thus, the total thickness of the inflation layers around the SUBOFF was matched to Prandtl's theoretical estimate of the turbulent boundary layer thickness over a flat plate [20] using $0.16L_S/Re_{L_S}^{1/7}$, where L_S is the surface length of the vehicle and Re_{L_S} has previously been defined.

4.2. Mesh independence study

The mesh independence studies were conducted to select the optimum mesh size that provides sufficiently accurate results while maintaining a low computational effort. The studies were first conducted for the pure sway manoeuvres to investigate the effects of the vehicles' surface and the surrounding mesh sizes on the interaction prediction. This research work utilized an unstructured mesh type and it is not possible to make completely systematic mesh refinements in unstructured meshes since the size of individual cells cannot be controlled directly [22]. Therefore, it is difficult to estimate the mesh uncertainty. However, four meshes (i.e. S1, S2, S3 and S4, where the S1 is the finest mesh and S4 is the coarsest) were generated by carrying out mesh refinements with an approximate refinement ratio of $\sqrt{2}$ and, the surge force, sway force and yaw moment solutions were obtained from each mesh. The finest mesh contained 4.86 million elements, while the coarsest mesh contained 1.49 million elements. Fig. 6 illustrates the maximum percentage difference of the force predictions from each mesh size compared to the results from the finest mesh. The computational time taken for each mesh size simulation is also provided. The mesh convergence and the mesh uncertainty were investigated according to the procedure recommended by [23,24]. The mesh convergence ratios (i.e. R_G) for the surge force, sway force and yaw moment calculated from the finest three (i.e. S1, S2 and S3) and the coarsest three (i.e. S2, S3 and S4), out of the four meshes were within the range of 0.56 and 0.67. The convergence is deemed to be achieved since the convergence ratios were within $0 < R_G < 1$ [23]. Therefore, the Richardson extrapolation [22,23] was used to estimate the mesh uncertainty. The estimated mesh uncertainties for the surge force, sway force and yaw moment were less than 1.6% of the S1 mesh solutions (i.e. the solutions from the finest mesh) and were less than 2.4% of the solutions from the S2 mesh. The S2 mesh (i.e. the 2.8 million element mesh) was selected as the optimum mesh since both the surge and sway force predictions were within 1% of the finest mesh force predictions (see Fig. 6) and within 2.4% of the corrected solutions. The selected mesh maintained around 53% less computational time compared to the finest mesh; i.e. run time reduced from 9.5 days to 4.5 days.

The mesh independence studies for the steady-state straight-line simulations were conducted by carrying out mesh refinements on the vehicle surfaces and the pressure interaction region between the vehicles. The finest mesh contained 6 million elements, while the coarsest mesh contained 1.2 million elements. The mesh convergences for the surge force, sway force and yaw moment were calculated similar to the pure sway simulations and were found to be within the converging range (i.e. $0 < R_G < 1$). The estimated mesh uncertainties were less than 2% of the solutions from the selected three million element mesh.

To ensure numerical accuracy and stability, all simulations were performed using a high order advection and second order backwards Euler transient scheme. Convergence was deemed achieved when solution residuals reduced to below 10^{-4} and reduced by more than three orders of magnitude using a maximum of 10 inner iteration loops per time step.

4.3. Time-step independence study

The dynamic simulations tend to fail if the utilized time-step was too large, since moving wall particles may cross more than one element per time-step and will pass their node solutions into an unknown element [19]. The largest possible time-step that could successfully carry-out the simulation for the selected mesh size was estimated to be 0.01 s. The influence of the simulation time-step was investigated by comparing the sway force responses for three time steps (i.e. 0.01 s, 0.008 s, and 0.006 s) with the predictions found to be relatively consistent with respect to the different time-steps (see Fig. 7). The maximum percentage difference between the sway force predictions for the time steps 0.01 s and 0.006 s was 0.4%. Therefore, a 0.01 s time-step was utilized for the simulations to reduce the simulation time. The spikes observed in force responses seen in Fig. 7 are due to the simulation initiations at re-mesh events, and are filtered out using a low pass filter.

5. Validation of numerical results

For validation purposes, the force responses obtained from CFD simulations were compared against those obtained from EFD. Fig. 8 shows the CFD and EFD sway force responses obtained from a two body pure sway motion test. It is seen that CFD and EFD responses vary in both magnitude and phase. The maximum magnitude deviation was below 5.58% for all validated cases.

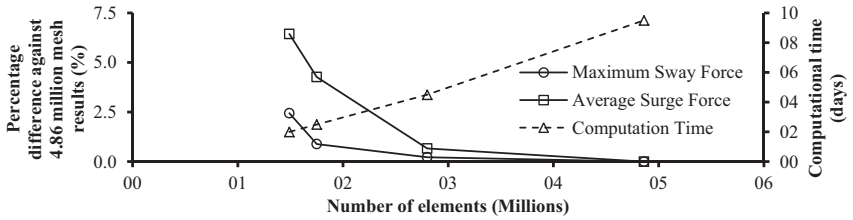

Fig. 6. Percentage uncertainty of the sway force and surge force with respect to the finest mesh.

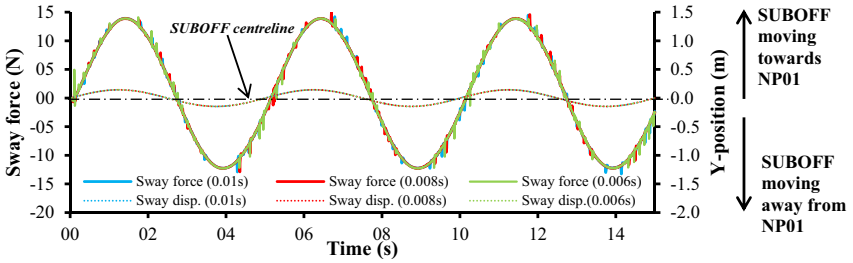

Fig. 7. Sway force responses for simulation time-steps of: 0.01 s, 0.008 s and 0.006 (note that the sway forces from the three time-steps coincide each other).

5.1. Phase difference between CFD and EFD sway force responses

A phase shift between the CFD and EFD force responses obtained from such Planner Motion Mechanism (PMM) tests and other similar tests is usually observed [25–28]. Whilst some predict that it is due to inaccurate initial conditions [25], others consider these to be possible experimental errors. However, this is an area of ongoing research. The minimum phase difference of 0.4% was seen at the lowest sway frequency (i.e. 0.05 Hz) and the maximum difference of 4.8% was observed at the highest sway frequency (i.e. 0.2 Hz). The phase difference between the CFD and EFD sway forces was directly proportional to the sway frequency. The effects of modelling uncertainties of the internal hollow section and the shell density of the SUBOFF are more significant at higher sway frequencies due to the higher acceleration. Thus, the phase uncertainty of CFD results could be partly due to the modelling uncertainties of the internal hollow region and internal free flood water section of the SUBOFF model. The other possible reasons for the difference could be an over prediction of the added mass within CFD and/or due to experimental errors. As the phase difference of the results are less than 5% for all the sampled frequencies and is within the experimental uncertainty, it was considered to have minimal effect to the main findings of the paper.

5.2. Validation of hydrodynamic coefficients between CFD and EFD results

In this section, the hydrodynamic coefficients derived through CFD results are compared against those obtained through EFD. The sway force coefficient due to sway acceleration ($Y_{\dot{v}}$) is derived using Eq. (4) from the sway forces recorded in-phase with displacement (i.e. Fy_{in} as shown in Fig. 8). A positive (+) displacement indicates that the lateral separation between the SUBOFF model and NP01 is less than that at the starting position and a negative (−) displacement indicates that the lateral separation between the models is larger than that at the starting position (for single body tests, this represents the SUBOFF model at the starboard and the port sides from the starting position respectively). The non-dimensionalized CFD & EFD force coefficients, recorded in-phase with displacement, are presented in Table 3. The forces were non-dimensionalized using Eq. (5),

$$\text{Non-dimensional sway force } (Fy') = \frac{2F}{\rho L^2 u^2} \tag{5}$$

where F is the force, ρ is the specific density of fresh water, L is the length of the model, and u is the surge velocity component.

It is seen that the CFD Fy'_{in} are in good agreement with EFD (with the greatest percentage difference of 5.4%) for sway frequencies of 0.2 Hz and 0.15 Hz. Even though the difference for 0.05 Hz is around 20%, the actual difference in forces predicted using CFD and those measured from EFD is smaller due to the lower frequency and is within the experimental bias error of ±0.2 N. For this reason, it is proposed that the numerical models can be used to obtain $y_{\dot{v}}$.

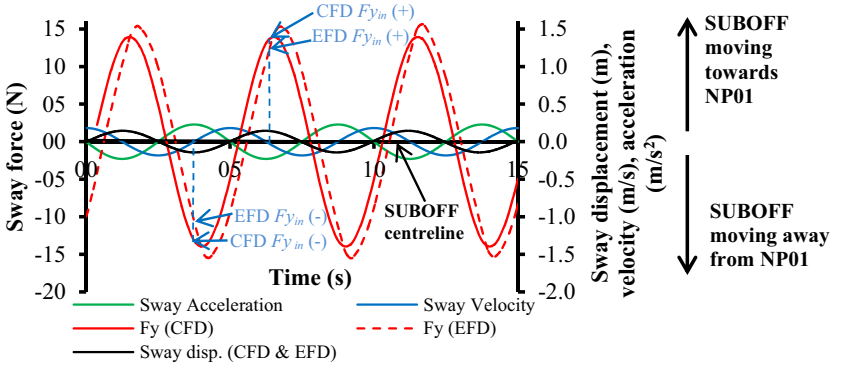

Fig. 8. CFD and EFD sway force responses for pure sway motion at 0.2 Hz.

Table 3
Variation of Fy'_{in} with sway frequency.

Frequency	CFD $Fy'_{in}(+)$	EFD $Fy'_{in}(+)$	Difference	CFD $Fy'_{in}(-)$	EFD $Fy'_{in}(-)$	Difference
0.2 Hz	0.0081	0.0077	5.4%	−0.0081	−0.0079	2.7%
0.15 Hz	0.0046	0.0048	3.2%	−0.0047	−0.0048	2.0%
0.05 Hz	0.0005	0.0006	18.0%	−0.0005	−0.0007	19.4%

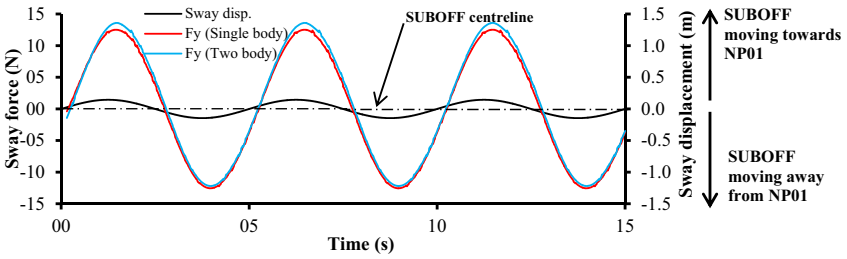

Fig. 9. Sway force responses for single and two body simulations (at R_{long} of 0 and R_{lat} of 1.829).

6. Results and discussion

The sway force response due to the pure sway motion of the SUBOFF model tested alone (termed as $Fy_{(SUBOFF)}$ in the following discussion) is a symmetric sinusoidal response along the time axis. Thus, the hydrodynamic coefficients (i.e. y_v and $y_{\dot{v}}$) derived from positive or negative displacement cycles of motion (i.e. when the SUBOFF model is on the starboard or port sides from its starting position respectively) are equal in magnitude (see Fig. 9). However, when the SUBOFF model is operating in proximity of the larger NP01 body, the sway force response is influenced by the interaction with the pressure field of the latter. Fig. 9 shows that the two body response is shifted towards the positive y-direction as compared to the single body response. The shift is not uniform (i.e. the interaction force is higher when the SUBOFF is closer to NP01). This is due to the increasing influence of the pressure field generated by the NP01 as the SUBOFF draws nearer, compared to that when the SUBOFF is further away. Due to the asymmetry of the two body sway force response; the hydrodynamic coefficients obtained from positive and negative displacement cycles are not equal in magnitude. Thus, the hydrodynamic coefficients of the SUBOFF, when moving towards and away from the NP01 are different.

6.1. Interaction forces and moments

With the aim of quantifying the interaction forces (i.e. $Fy_{(interaction)}$) acting on the SUBOFF model due to the pressure of the larger body, the interaction forces are defined as,

$$Fy_{(two\ \ body)} = Fy_{(SUBOFF)} + Fy_{(interaction)} \quad (6)$$

The interaction sway force was non-dimensionalized to obtain the interaction sway force coefficient using Eq. (5) by substituting $Fy_{(two\ body)}$ as the force.

6.1.1. Interaction sway force against lateral separation

The variation of the isolated interaction force coefficient when the SUBOFF model is moving towards and away from the larger body is plotted against the sway displacement in Fig. 10. For all the analyzed cases, the interaction force when the SUBOFF is moving away from the larger body was observed to be higher than when it is moving towards it. Fig. 11 shows that a low pressure field is generated throughout the span of the larger body, which becomes significant in the regions with longitudinally curved surfaces (i.e. just after the bow and just before the stern). When the SUBOFF model sways while moving forward, a low pressure region is generated at the opposite side to the SUBOFF's sway direction. In Fig. 11(a) when the SUBOFF model moves towards the larger body, the low pressure fields due to the larger body and the SUBOFF's sway motion are at opposite sides of the SUBOFF. Thus, the interaction sway force due to resultant pressure field is lower, as the SUBOFF's pressure field due to the sway motion is opposing the interaction force of the NP01. However, when the model moves away from the larger body as seen in Fig. 11(b), the low pressure fields due to the larger body and the SUBOFF's sway motion are both in between the two bodies. Thus, the SUBOFF's own pressure field complements the interaction sway force, resulting in a higher attraction force.

6.1.2. Interaction sway force and yaw moment against longitudinal separation

The variation of the interaction sway force and yaw moment coefficients against the longitudinal separation of the two bodies are shown in Figs. 12 and 13 respectively. The forces and moments were recorded at positive peaks of the sway displacement (i.e. when the SUBOFF is closest to the NP01 model during each cycle). The sway forces were quantified for three sway frequencies of 0.2 Hz, 0.15 Hz and 0.05 Hz. The yaw moment was calculated at a reference point where the single body yaw moment reached zero (i.e. 0.701 m aft of the SUBOFF nose tip). Therefore, the yaw moment shown in Fig. 13 is purely due to the interaction with the larger body. The positive yaw moment represents the SUBOFF bow attempting to

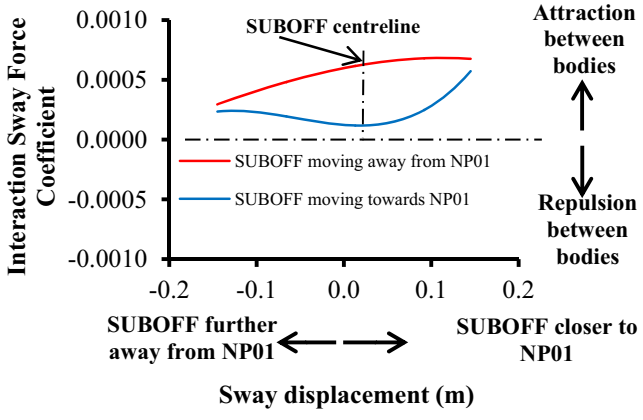

Fig. 10. Interaction sway force coefficient against sway displacement (at R_{long} of 0).

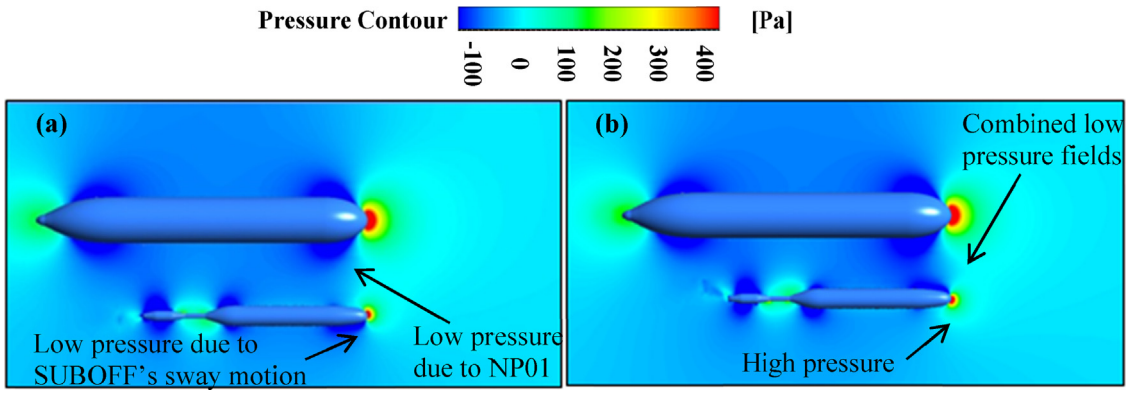

Fig. 11. Visualization of the predicted two-body pressure interaction field with (a) the SUBOFF moving towards NP01 and (b) the SUBOFF moving away from NP01 (at R_{long} of 0 and R_{lat} of 1.829).

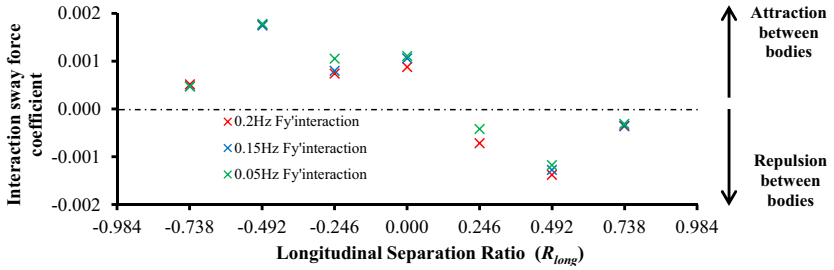

Fig. 12. Interaction sway force coefficient due to sway acceleration vs. R_{long} (at R_{lat} of 1.475, sway amplitude of 0.145 m and sway frequency of 0.2 Hz).

yaw towards the NP01 as shown in Fig. 1(a). The yaw moment was non-dimensionalized using Eq. (7),

$$\text{Non-dimensional yaw moment } (N') = \frac{2N}{\rho L^3 u^2} \tag{7}$$

where N is the yaw moment, ρ is the specific density of fresh water, L is the length of the model, and u is the surge velocity component.

Fig. 14 illustrates the pressure visualization with longitudinal separation. When R_{long} is −0.737, the SUBOFF nose tip reaches the low pressure region around the aft section of the NP01 model. Furthermore, the confined area between the SUBOFF bow and the NP01 causes an increase in the flow velocity between the two bodies, resulting in the intensification of the low pressure field (in accordance with Bernoulli's theorem). The low pressure field between the two bodies attracts the SUBOFF towards the NP01 (i.e. a positive interaction force as shown in Fig. 12). However, the stern of the SUBOFF is still within the relatively higher pressure region aft of the NP01. Thus, the combination of the high and low pressure fields acting on the stern and forward regions of the SUBOFF respectively results a positive yaw moment as shown in Fig. 13 (i.e. a moment acting on the SUBOFF yawing its bow towards the larger body).

When R_{long} is −0.491, the entire SUBOFF model is within the low pressure interaction field created by the aft section of the NP01. Furthermore, the restricted space between the two bodies creates a second low pressure field along the length of the SUBOFF. These two low pressure fields attract the SUBOFF towards the NP01, causing the highest attraction force. However, the yaw moment is relatively small as both the bow and the stern of the SUBOFF are attracted towards the NP01 model.

When R_{long} is −0.246, the SUBOFF is located within the mid-body region of the larger NP01 model. The intensity of the low pressure field due to the NP01 reduces in this region due the parallel mid-body section. However, the low pressure created due to the accelerated flow field between the two bodies attracts the SUBOFF towards the NP01, producing the lowest interaction force. The SUBOFF bow is attracted towards the NP01 due to the low pressure field created at the bow of the NP01, resulting in a positive yaw moment.

The attraction force again increases when the R_{long} is 0, due to the increase in the low pressure field located just aft of the bow of the larger body. The SUBOFF bow is pushed away from the NP01 by the high pressure field around the stagnation point of the latter, while the SUBOFF stern is attracted towards the NP01, resulting in a negative yaw moment.

As the SUBOFF moves further along the length of NP01 to a R_{long} of 0.246, the bow of the SUBOFF model moves into the high pressure

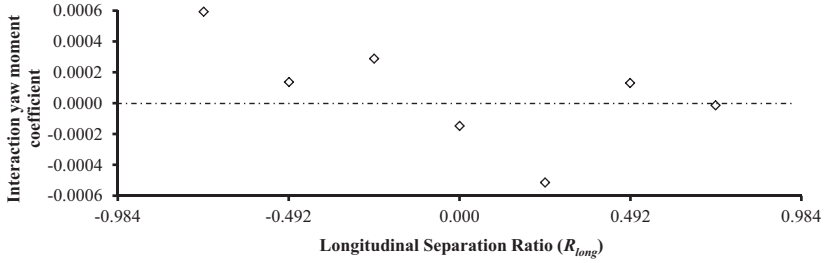

Fig. 13. Interaction yaw moment coefficient vs. R_{long} (at R_{lat} of 1.475, sway amplitude of 0.145 m and sway frequency of 0.2 Hz).

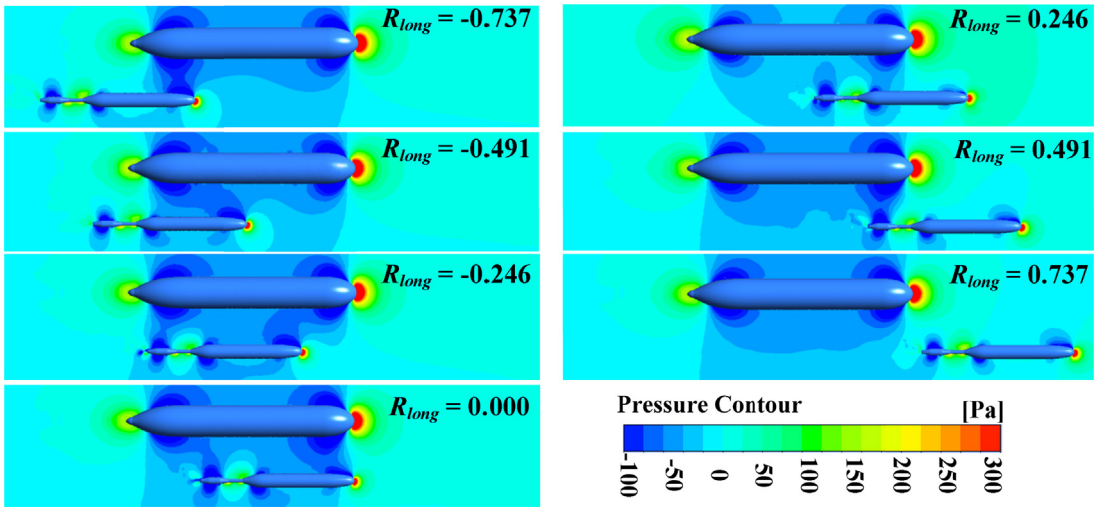

Fig. 14. Pressure visualization for different R_{long} (at R_{lat} of 1.829).

region around the stagnation point of the NP01, which pushes the bow of the SUBOFF further away from the larger body, The stern of the SUBOFF is pulled towards the NP01 by the low pressure field located just after the bow of the latter. This results in an overall negative sway force and a yaw moment.

When R_{long} is +0.491, the entire SUBOFF is within the forward high pressure region, causing the highest repulsive interaction force. The stern of the SUBOFF is pushed away from the NP01 due to the high pressure region at the stagnation point of the NP01 causing a slightly positive yaw moment. When R_{long} is 0.737 the smaller body moves further away from the high pressure region, progressively reducing the repulsive interaction sway force as well as the positive yaw moment.

Although the trends of interaction force variations for the three frequencies shown in Fig. 12 are similar, their magnitudes do vary as much as 24%, especially when the two bodies are alongside. This shows that the interaction force is frequency dependent.

6.1.3. Interaction surge force

A similar analysis was carried out for the interaction surge force ($Fx_{(interaction)}$), which varies with the sway displacement and the direction of sway (i.e. whether towards or away from the larger body). However, unlike the interaction sway force, the interaction surge force is higher when R_{long} is below 0.246 and the SUBOFF model is moving away from the larger body than when moving towards it, but opposite when R_{long} is above 0.246 (see Fig. 15).

According to the pressure visualizations shown in Fig. 14, at R_{long} of −0.737 and −0.491, a low pressure region is located ahead the SUBOFF, effectively reducing the drag force. Thus, when R_{long} is lower than −0.491, the drag force acting on the SUBOFF model due to the interaction with the larger body is lower than the drag force for the single body (see Fig. 15). When the R_{long} is higher than −0.246, the high pressure region located forward of the SUBOFF model increases the drag force, resulting in it being greater than the single body drag force. Leong et al. [6] investigated the steady state surge force acting on the SUBOFF model when operating in close proximity to the NP01, and concluded that it is unaffected by the larger body when the R_{long} is above 1.02 and below −1.19.

The above results indicate that the hydrodynamic coefficients of an AUV vary with the influence of interactions caused by third party objects; in this case a larger moving body. However, similar outcomes could be expected for other types of boundaries such as jetty walls, seabed, and surface ice layers [29,30].

6.2. Proposed simplified method to predict interaction sway force

A simplified method was developed to obtain the two body hydrodynamic coefficients using single body hydrodynamic coefficients and steady-state interaction force due to straight-line motion. The inverse of this approach was also validated, i.e. obtaining the steady-state interaction force from two body hydrodynamic coefficients. The following section introduces the method, its validation and limitations.

6.2.1. Simplified method: obtaining the two body hydrodynamic sway forces

A new term called the 'quasi-static' sway force is defined by adding the steady-state interaction force due to straight-line motion to the single body pure sway force as shown below,

$$Fy_{(quasi\text{-}static)} = Fy_{(two\ \ body,\ \ steady\ \ state)} + Fy_{(single\ \ body,\ \ dynamic)} \quad (8)$$

where $Fy_{(two\ body,\ steady\ state)}$ – steady state sway force on the smaller body due to straight-line forward motion of the two bodies together.* $Fy_{(single\ body,\ dynamic)}$ – sway force on the smaller body obtained from single body pure sway motion.* (*The lateral separation ratio of the tests should be maintained at the ratio at which the quasi-static sway force is required.)

The quasi-static sway forces are compared against the sway forces obtained from two body pure sway motion tests (i.e. $Fy_{(two\ body,\ dynamic)}$) in Fig. 16. The sway forces were recorded in phase with displacement (i.e. the sway force due to sway acceleration). The positive (+) and negative (−) signs indicate that the forces were measured when the SUBOFF model is closer or further away from the centreline of motion to the larger NP01 body respectively. The maximum percentage difference between $Fy_{(quasi\text{-}static)}$ and $Fy_{(dynamic)}$ is below 14% for all the test cases. Therefore, it could be deduced that the quasi-static sway force ($Fy_{(quasi\text{-}static)}$) is a good indicator of the two body dynamic sway force acting on the smaller body ($Fy_{(two\ body,\ dynamic)}$).

Using this method, the hydrodynamic coefficients of an AUV when operating close to a larger body could be estimated by simply adding the steady-state interaction force coefficients (obtained from Eqs. (3) and (4) by substituting Fy_{out} and Fy_{in} with the steady-state force) into the single body hydrodynamic coefficients (i.e. $Y_{\dot{v}}$ and Y_v). Therefore, the variation of hydrodynamic coefficients due to a second body could be estimated by conducting a cost effective steady-state simulation, rather than time intensive dynamic pure sway motion simulations. This method might also be valid

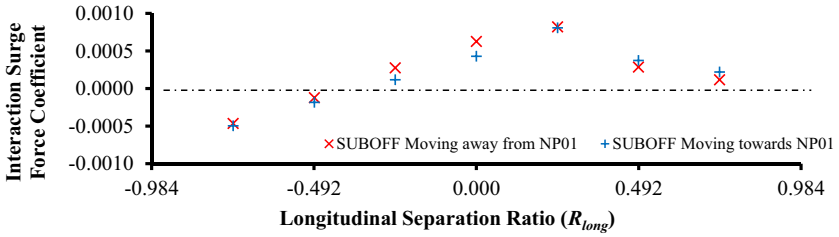

Fig. 15. Interaction surge force coefficient vs. R_{long} (at R_{lat} of 1.475, sway amplitude of 0.145 m and sway frequency of 0.2 Hz).

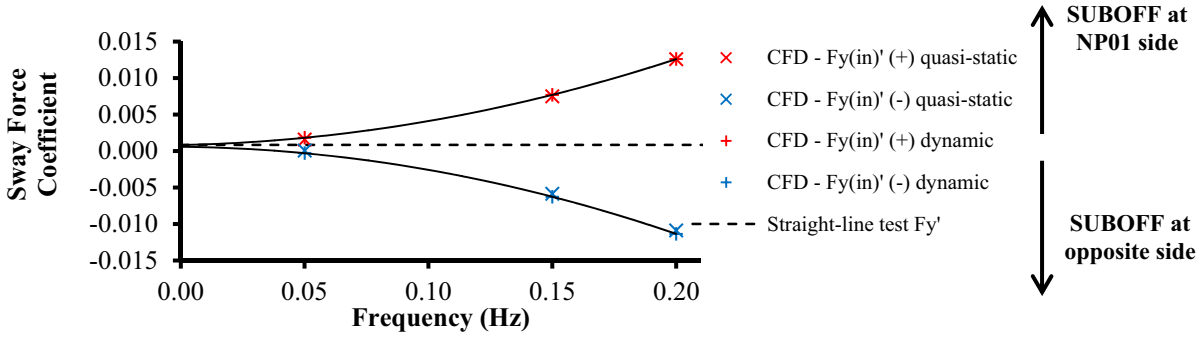

Fig. 16. Comparison of quasi-static and dynamic Fy'_{in}.

for when the AUV is manoeuvring near other types of stationary boundaries such as sea-bed, wall boundaries, and under ice layers, and is worth investigating since the method will save time. However, the proposed method has the following limitations:

- the sway frequency and amplitude of the single body pure sway motion tests should be the same as the sway frequency and amplitude of the required $Fy_{(quasi\text{-}static)}$;
- the lateral body separations of the measured $Fy_{(steady\ state)}$ and $Fy_{(single\ body,\ dynamic)}$ should be equal to the lateral body separation of the required $Fy_{(quasi\text{-}static)}$; and
- the proposed quasi-static approach is validated only for the range shown in Table 2.

6.2.2. *Inverse of the simplified method: obtaining the steady-state interaction sway force*

Inverse of the above simplified method is to obtain the two body steady-state interaction force due to straight-line motion using the sway forces obtained from two body pure sway motion tests. The second order polynomial extrapolation of $Fy_{(two\ body,\ dynamic)}$ meets the steady-state interaction force at the sway frequency of 0 Hz (see Fig. 16), with a percentage variation of less than 8%. Similar patterns were observed in all the analyzed cases. Therefore, this method could be used to obtain the steady-state interaction sway force due to forward motion at any lateral separation (within the sway amplitudes) using a set of pure sway motion tests and this method is an efficient way of obtaining the steady-state interaction force at multiple lateral separations. The limitations of this method are as follows:

- validations is limited to the range shown in Table 2; and
- the steady-state interaction forces obtained from the current study are relatively small due to the small body diameter ratio between the two models, thus, the accuracy of the proposed method needs to be further validated by replicating the study for models having a larger body diameter ratio.

7. Conclusions

An investigation into the hydrodynamic interaction between an AUV operating in close proximity to a larger moving vehicle such as a submarine was conducted, with the development of a CFD model to replicate the pure sway motion of the AUV under these conditions. The model was validated through physical experimental work conducted using an AUV model fitted to an HPMM and a larger adjacent body moving along the axial direction in AMC's Towing Tank. The percentage difference between the CFD and EFD sway forces were generally below 6% and within the experimental error margins.

The maximum hydrodynamic interaction sway force acting on the smaller body due to the presence of the larger NP01 body was found to be an attraction force when the former is located behind the nose of the latter (i.e. when the longitudinal separation ratio is below zero) and vice versa. This was due to the low pressure field created around the span and the high pressure field created around the nose region of the larger body. The lowest interaction between the two bodies occurred when the smaller body is located around the midship section of the larger body. Furthermore, the interaction sway force coefficient when the SUBOFF is moving towards the NP01 was found to be lower than that when it is moving further apart due to the low pressure field created around the span of the larger body.

The proposed simplified method is able to estimate the hydrodynamic coefficients of an AUV when operating close to a larger underwater body by simply adding the steady-state interaction force coefficient to the single body hydrodynamic coefficient, with a maximum percentage variation of 14%. Therefore, the variation of hydrodynamic coefficients due to a second body could be estimated by conducting a cost effective steady-state simulation, rather than time intensive dynamic pure sway motion simulations. The inverse of this method is able to provide an approximation of the steady-state interaction force at any lateral separation (within the amplitudes of the pure sway motion tests) using the two body sway force due to pure sway motion with a maximum percentage variation of 8%. This method is an efficient way of obtaining the steady-state interaction force at multiple lateral separations.

References

[1] Kemna S, Hamilton MJ, Hughes DT, LePage KD. Adaptive autonomous underwater vehicles for littoral surveillance. Intell Serv Robot 2011;4:245–58.
[2] Forrest AL, Laval BE, Pieters R, Lim DS. Convectively driven transport in temperate lakes. Limnol Oceanogr 2008;53:2321.
[3] Rodgers J, Wharington J, Tynan A, Coxhead M. A concept for the deployment of unmanned maritime systems from submarines: MURULA integration impact modelling and results; 2008.
[4] Osterloh C, Meyer B, Amory A, Pionteck T, Maehle E. MONSUN II—towards autonomous underwater swarms for environmental monitoring. In: International conference on intelligent robots and systems (IROS2012), workshop on robotics for environmental monitoring. 2012. p. 7–12.
[5] Hardy T, Barlow G. Unmanned Underwater Vehicle (UUV) deployment and retrieval considerations for submarines. In: 9th international naval engineering conference and exhibition. 2008.
[6] Leong Z, Saad K, Ranmuthugala S, Duffy J. Investigation into the hydrodynamic interaction effects on an AUV operating close to a submarine. In: Pacific 2013 international maritime conference. 2013. p. 1–11.
[7] Duffy J, Renilson M. The importance of the form of time domain forces on berthed ship interaction. In: The second international conference on manoeuvring in shallow & confined waters: ship to ship interaction. 2011. p. 107–16.
[8] Lataire E, Vantorre M, Delefortrie G, Candries M. Mathematical modelling of forces acting on ships during lightering operations. Ocean Eng 2012;55:101–15.
[9] Vantorre M, Verzhbitskaya E, Laforce E. Model test based formulations of ship–ship interaction forces. Ship Technol Res 2002;49:124–41.
[10] Mawby A, Wilson P, Bole MP, Duncan FSJ. Manoeuvring simulation of multiple underwater vehicles in close proximity. Hamburg: Ministry of Defence, Defence Procurement Agency; 2006.
[11] Leong ZQ. CFD simulations of multiple submerged bodies in relative motion for control systems. Launceston: National Centre for Maritime Engineering and Hydrodynamics; 2013.
[12] Groves NC, Huang TT, Chang MS. Geometric characteristics of DARPA (Defense Advanced Research Projects Agency) SUBOFF models (DTRC Model Numbers 5470 and 5471). DTIC document; 1989.
[13] ITTC. ITTC – recommended procedures and guidelines: full scale measurements speed and power trials instrumentation installation and calibration. In: International towing tank conference. 2011.
[14] Lewis EV. Principles of naval architecture – volume III. Motion in waves and controllability. The Society of Naval Architects and Marine Engineers; 1989.
[15] Hama FR. An efficient tripping device. J Aeronaut Sci 1957;24:236–7.
[16] Steel V. Investigation into the effect of wave making on a submarine approaching the free surface. Launceston: University of Tasmania; 2010.
[17] van Barneveld W. Experimental investigation into the interactions between two underwater bodies. Launceston: University of Tasmania; 2013.
[18] Leong ZQ, Ranmuthugala D, Penesis I, Nguyen H. RANS-based CFD prediction of the hydrodynamic coefficients of DARPA SUBOFF geometry in straight-line and rotating arm manoeuvres. Trans R Inst Nav Archit Part A Int J Marit Eng 2015 [accepted].
[19] Leong ZQ, Ranmuthugala D, Penesis I, Nguyen HD. Computational fluid dynamics re-mesh method to generating hydrodynamic models for maneuvering simulation of two submerged bodies in relative motion. J Comput Sci Cybern 2012;27:353–62.
[20] White FW. Fluid mechanics. 7th ed. New York: McGraw-Hill; 2011.
[21] Tu J, Inthavong K, Ahmadi G. Computational fluid and particle dynamics in the human respiratory system. Springer; 2012.
[22] Simonsen C, Otzen J, Klimt C, Larsen N, Stern F. Maneuvering predictions in the early design phase using CFD generated PMM data. In: 29th symposium on naval hydrodynamics. 2012.
[23] Stern F, Wilson RV, Coleman HW, Paterson EG. Comprehensive approach to verification and validation of CFD simulations—Part 1: Methodology and procedures. J Fluids Eng 2001;123:793–802.
[24] Wilson RV, Stern F, Coleman HW, Paterson EG. Comprehensive approach to verification and validation of CFD simulations—Part 2: Application for RANS simulation of a cargo/container ship. J Fluids Eng 2001;123:803–10.
[25] Sakamoto N, Carrica PM, Stern F. URANS simulations of static and dynamic maneuvering for surface combatant: Part 1. Verification and validation for forces, moment, and hydrodynamic derivatives. J Mar Sci Technol 2012;17:422–45.
[26] ITTC. ITTC – recommended procedures and guidelines: guideline on use of RANS tools for manoeuvring prediction. In: International towing tank conference. 2011.
[27] Carrica PM, Ismail F, Hyman M, Bhushan S, Stern F. Turn and zigzag maneuvers of a surface combatant using a URANS approach with dynamic overset grids. J Mar Sci Technol 2013;18:166–81.
[28] Górnicz T, Kulczyk J. Application of CFD methods for the assessment of ship manoeuvrability in shallow water. Methods Algorithms Navig: Mar Navig Saf Sea Transp 2011:P45–50.
[29] Ananthakrishnan P. AUV hydrodynamics in shallow water during adverse weather conditions. DTIC document; 1998.
[30] Ananthakrishnan P, Zhang K-Q. AUV motion in a wave field. In: OCEANS'98 conference proceedings: IEEE. 1998. p. 1059–63.